Quarter-Car Experimental Study for Series Active Variable Geometry Suspension

Min Yu, *Student Member, IEEE*, Carlos Arana, Simos A. Evangelou, *Senior Member, IEEE*, and Daniele Dini

***Abstract*— In this paper, the recently introduced series active variable geometry suspension (SAVGS) for road vehicles is experimentally studied. A realistic quarter-car test rig equipped with double-wishbone suspension is designed and built to mimic an actual grand tourer real axle, with a single-link variant of the SAVGS and a road excitation mechanism implemented. A linear equivalent modeling method is adopted to synthesize an H-infinity control scheme for the SAVGS, with the geometric nonlinearity compensated. Simulations with a theoretical nonlinear quarter-car indicate the SAVGS potential to enhance suspension performance, in terms of ride comfort and road holding. Practical features in the test rig are further considered and included in the nonlinear model to compensate the difference between the theoretical and testing behaviors. Experiments with a sinusoidal road, a smoothed bump and hole, and a random road are performed to evaluate the SAVGS practical feasibility and performance improvement, the accuracy of the model, and the robustness of the control schemes. Compared with the conventional passive suspension, ride comfort improvements of up to 41% without any deterioration of the suspension deflection are demonstrated, while the SAVGS actuator power is kept very low, at levels below 500 W.**

***Index Terms*— Active suspension, model validation, quarter-car test rig, robust control application, variable geometry.**

I. Introduction

VEHICLE suspension is a system of springs, shock absorbers, and arms which connects a car body to its wheels and allows relative motion between the two [1]. Suspensions are widely studied to improve ride comfort and road holding. According to the nature of the force-producing elements, suspension designs are classified into three main types [2], [3].

1) *Passive Suspension:* The main component is a conventional spring-damper unit, which passively adapts to the road profile and dissipates energy from road perturbations. This type of suspension still dominates the market due to low cost and easy maintenance.
2) *SemiActive Suspension:* The structure is similar to a passive suspension but the damping force is actively adjusted by electro-rheological, or magneto-rheological dampers, or solenoid valve controlled dampers.
3) *Parallel Active Suspension:* A separate (hydraulic, hydropneumatic, or electromagnetic) actuator is employed in parallel with a passive spring or spring-damper unit to exert an independent force and provide improved performances. The performance of active suspensions can be further improved and realize its full potential by integration of advanced sensors and intelligent controls, such as road preview control [4].

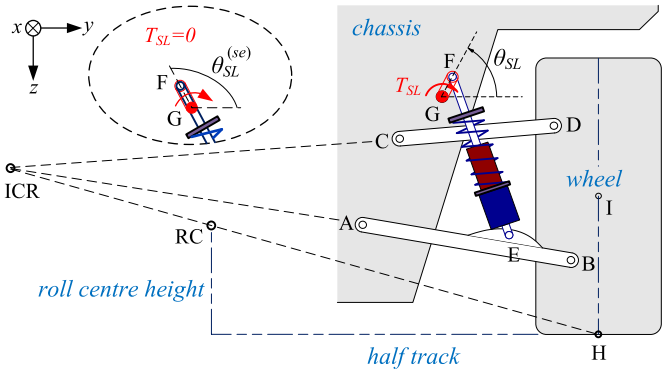

Fig. 1. SAVGS application to a quarter-car with double-wishbone suspension. "*RC*" is the vehicle roll center, and "ICR" is the instantaneous center of rotation. θ_{SL} is the single-link angle with respect to the horizontal plane. The superscript (se) denotes the static equilibrium state with zero torque (T_{SL}) applied on the single link [6].

More recently, a series active variable geometry suspension (SAVGS) has been proposed and theoretically proven as a valid alternative to existing solutions [5]–[12]. Fig. 1 illustrates the SAVGS application to a quarter-car with a double-wishbone suspension. In addition to a conventional suspension assembly, a single-link arm is introduced between the chassis (point "G") and the upper end eye of the spring-damper unit (point "F"). The single-link is driven by a rotary actuator to actively improve the vehicle dynamics. The SAVGS features are as follows:

1) performance improvement in ride comfort and road holding (with additional improvements available in the full-car case);

Manuscript received March 28, 2017; revised August 5, 2017; accepted November 1, 2017. Date of publication December 28, 2017; date of current version February 8, 2019. Manuscript received in final form November 6, 2017. This work was supported in part by the U.K. Engineering and Physical Sciences Research Council under Grant EP/G006477/1, in part by Imperial Innovations, and in part by China Scholarship Council under Grant 201406320205. Recommended by Associate Editor K. Butts. *(Corresponding author: Min Yu.)*

M. Yu and S. A. Evangelou are with the Department of Electrical and Electronic Engineering, Imperial College London, London SW7 2AZ, U.K. (e-mail: m.yu14@imperial.ac.uk; s.evangelou@imperial.ac.uk).

C. Arana is with the Departments of Electrical and Electronic, and Mechanical Engineering, Imperial College London, London SW7 2AZ, U.K. (e-mail: carlos.arana-remirez10@imperial.ac.uk).

D. Dini is with the Department of Mechanical Engineering, Imperial College London, London SW7 2AZ, U.K. (e-mail: d.dini@imperial.ac.uk).

Color versions of one or more of the figures in this paper are available online at http://ieeexplore.ieee.org.

Digital Object Identifier 10.1109/TCST.2017.2772912

This work is licensed under a Creative Commons Attribution 3.0 License. For more information, see http://creativecommons.org/licenses/by/3.0/

2) limited power demand in the single-link actuator;
3) small sprung mass increment and negligible unsprung mass increment;
4) inherent fail-safe behavior [6].

An experimental study of the SAVGS with a quarter-car test rig is performed in this paper, with the main contributions being: 1) mechatronic system development of the SAVGS quarter-car test rig; 2) H-infinity control with geometric nonlinearity compensated and sensor noise penalized, for operating the SAVGS; and 3) experimental validation of the SAVGS practical feasibility, the modeling accuracy, and the robustness of the control algorithms.

A variety of quarter-car test rigs have been set up for active suspensions study [13]–[22], as experiments are highly important to evaluate the practical implementation feasibility and control system robustness. However, two primary limitations often exist in these test rigs. First, both the sprung and unsprung masses perform pure vertical motions, without accommodating the suspension kinematics (e.g., the installation ratio [23] and the lateral tire force). Second, parameters of realistic quarter cars (e.g., the spring stiffness and the sprung mass) are scaled down, and therefore the actual practical feasibility cannot be accurately evaluated. The test rig built in this paper aims to address both of these issues.

The remainder of this paper is organized as follows. Section II presents the mechanical design and implementation of an SAVGS quarter-car test rig, including the design of the single-link and road excitation mechanisms. Section III describes the control systems involved, in terms of both theoretical design and physical implementation. This includes: an adoption of a linear equivalent modeling method to synthesize an (outer-loop) H-infinity control scheme for the single-link operation, the design of (inner-loop) actuator control, and the embedded system development in the rig for the overall control implementation. Section IV analyzes the SAVGS test rig by simulations with a theoretical nonlinear quarter-car model, and further develops this model to account for practical features of the test rig. Section V conducts quarter-car experiments over a sinusoidal road, a smoothed bump and hole, and a random road, and analyzes the results. Conclusions are drawn in Section VI.

II. Quarter-Car Test Rig Development

This section presents the mechanical design and implementation of the SAVGS quarter-car test rig. The baseline rig is built from an actual conventional passive double-wishbone suspension arrangement connecting an actual wheel (unsprung mass) to a set of steel plates (sprung mass) supported on a frame structure with a rail and carriage guiding system that allows only vertical motion of the plates. The active single-link with its actuation and transmission mechanism is then integrated, as well as a horizontal plate with a vertical excitation mechanism, which emulate road disturbances on the wheel. The suspension response is measured by related sensors. The mass properties and the spring-damper characteristics are in accordance with those in one quarter of a grand tourer (GT). The mechanical parameters of the GT quarter car, adopted by the rig, are listed in Table I.

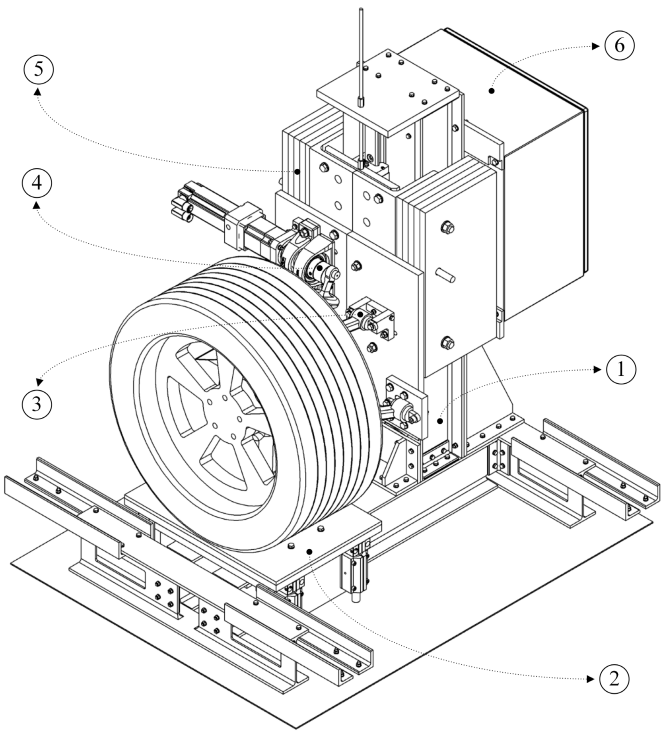

Fig. 2. Isometric view of the SAVGS quarter-car test rig showing 1) supporting frame, 2) excitation mechanism, 3) double-wishbone suspension assembly, 4) single-link, 5) sprung mass, and 6) electrical equipment cabinet.

The isometric view of the SAVGS quarter-car test rig is shown in Fig. 2. The development procedure comprises three stages: 1) the dimensioning of the suspension passive geometry; 2) the integration of the active single-link mechanism; and 3) the design of the road excitation mechanism.

A. Dimensioning of Passive Suspension

The double-wishbone suspension assembly utilized is from the rear axle of a Ferrari F430. It mainly comprises: one spring-damper unit (Öhilins TTX40), one set of double-wishbone arms, and one hub carrier and its attached road wheel.

This assembly is constructed in the rig according to its conventional geometric arrangement, and therefore it can accurately emulate the actual suspension operation in a GT. The geometric parameters are listed in Table II, where the position of the roll center [23] is governed by the customized car body size with rolling and pitching stability taken into account, the static wheel camber angle is determined by the desired lateral force, and the installation ratio is mainly decided by the desired suspension stiffness and required suspension travel. These parameters are taken from Ferrari car datasheets, while the position of points "A," "C," and "G" (see Fig. 1) in the passive case is to be determined.

First, the cylindrical joints connecting the wishbones and the sprung mass (points "A" and "C") are dimensioned as follows.

1) With the given roll center height (l_{rc}), half-track width (l_{ht}) and initial wheel camber angle (θ_{IHy}), points "B," "D," "I," "H" at their static equilibrium can be fixed.

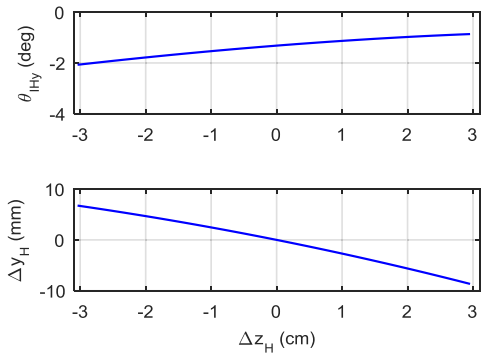

Fig. 3. Changes in the camber angle (top) and the scrub displacement (bottom) throughout the wheel travel.

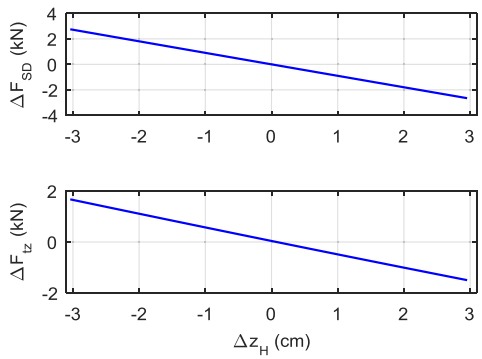

Fig. 4. Changes in the spring force (top) and the vertical tire force (bottom) throughout the wheel travel, with the sprung mass assumed to be fixed.

2) Due to the fact that the wheel motion is constrained by both the upper and the lower wishbones, lines of "A–B," "C–D," and "RC–H" intersect at the point "ICR" (commonly referred to as instantaneous center of rotation) [23]. With this assumption, the position of "A" and "C" can be determined by an appropriate value of $l_{\mathrm{ICR-H}}$ (the distance between point "H" and "ICR").
3) The suspension geometric arrangement also aims to minimize the changes in both the camber angle (θ_{IHy}) and the scrub displacement (Δy_H) throughout the possible wheel travel (Δz_H), so that the tire attitude can maintain the desired lateral handling ability (e.g., cornering action).

By sweeping the value of $l_{\mathrm{ICR}-H}$, the position of the points "A" and "C" can be determined with the minimal camber and scrub variation obtained. The corresponding wheel motion with the optimized $l_{\mathrm{ICR}-H}$ (=2.92 m) is shown in Fig. 3, in which the camber angle (θ_{IHy}) and the scrub displacement (Δy_H) vary only slightly within [−2.07°, −0.86°] and [−8.7 mm, +6.8 mm], respectively.

Second, the cylindrical joint connecting the damper's upper end eye and the sprung mass ("G" in Fig. 1, in the passive case there is no single-link and point "F" collapses to "G") is positioned as follows.

The installation ratio at the static equilibrium (se) is given by

$$R_{\mathrm{SD}}^{(\mathrm{se})} = \left.\frac{dl_{\mathrm{SD}}}{dz_H}\right|_{(\mathrm{se})} \tag{1}$$

and its value is taken from the vehicle manufacturer datasheet ($R_{\mathrm{SD}} = 0.56$). By applying the principle of virtual work to the unsprung mass (m_u) at its static equilibrium configuration, we obtain

$$F_{\mathrm{SD}}^{(\mathrm{se})}\delta l_{\mathrm{SD}} + m_u g \delta z_I = F_{\mathrm{tz}}^{(\mathrm{se})}\delta z_H. \tag{2}$$

The equilibrium spring force $F_{\mathrm{SD}}^{(\mathrm{se})}$ and vertical tire force $F_{\mathrm{tz}}^{(\mathrm{se})}$ can be further written as

$$\begin{aligned} F_{\mathrm{SD}}^{(\mathrm{se})} &= k_{\mathrm{SD}}\left(l_{\mathrm{SD0}} - l_{\mathrm{SD}}^{(\mathrm{se})}\right) \\ F_{\mathrm{tz}}^{(\mathrm{se})} &= (m_s + m_u)g. \end{aligned} \tag{3}$$

Combining (1)–(3), the equilibrium spring-damper length $l_{\mathrm{SD}}^{(\mathrm{se})}$(= 0.354 m) and angle $\theta_{\mathrm{SD}}^{(\mathrm{se})}$(= 63.6°, with respect to the horizontal plane) can be determined, and therefore the location of point "G" is found.

This subsection fully defines the geometric arrangement of the double-wishbone suspension in the passive case. The changes in the spring force (ΔF_{SD}) and the vertical tire force (ΔF_{tz}) with respect to the wheel travel are illustrated in Fig. 4.

B. Design of Single-Link Mechanism

The single-link mechanism is introduced with the suspension geometric arrangement (at the static equilibrium) unchanged.

The single-link length of 11 mm has been selected for the rear axle of the GT [6], with the desired tire force increment and the actuator torque-speed envelope considered. The single link can be stabilized at different angles by an equilibrium torque T_{SL} from the single-link actuator. This torque is calculated by applying the virtual work principle to the single link

$$T_{\mathrm{SL}}\delta\theta_{\mathrm{SL}} = F_{\mathrm{SD}}\delta l_{\mathrm{SD}}. \tag{4}$$

With the sprung mass position assumed to be fixed, the single-link influence on the vertical tire force and the spring force is shown in Fig. 5. It can be seen that this SAVGS configuration is reasonable when compared with the results in Fig. 4, as the single-link rotation has the potential to compensate the tire force changes (ΔF_{tz}) caused by the wheel travel propagation. Moreover, the SAVGS with the single link at an offset angle ($\Delta\theta_{\mathrm{SL}}$) of 90° (referred to as the nominal state) has more effective performance influence, as both the spring force (ΔF_{SD}) and vertical tire force increment (ΔF_{tz}) against the single-link angle ($\Delta\theta_{\mathrm{SL}}$) have the maximum slope. The essential steady-state load analysis of the SAVGS and the calculation of the steady-state T_{SL} also help to guide the selection of the single-link actuator, as well as the following structural design.

Fig. 6 illustrates the mechanical arrangement of the single link and its transmission assembly. Inspired by the "engine crankshaft," the single link is integrated with the transmission shaft (accommodated by two bearings) via a "crankpin" with an offset of $l_{\mathrm{SL}} = 11$ mm. This "crankpin" acts as point "F" (see in Fig. 1), which is aligned with the upper end eye of the

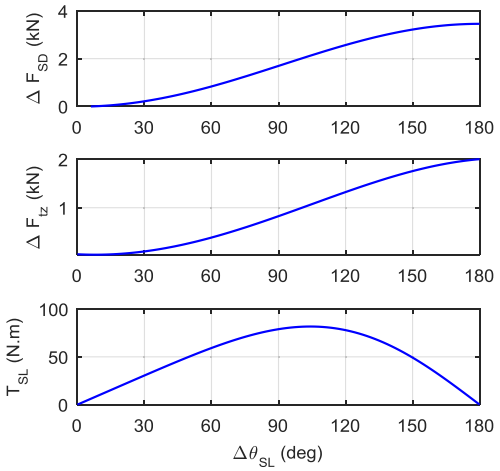

Fig. 5. Changes in the spring force (top), the vertical tire force (middle), and the single-link torque (bottom) with respect to the single-link angle. The sprung mass is assumed to be fixed. $\Delta\theta_{\mathrm{SL}}$ is the single-link angle increment with respect to its static equilibrium state.

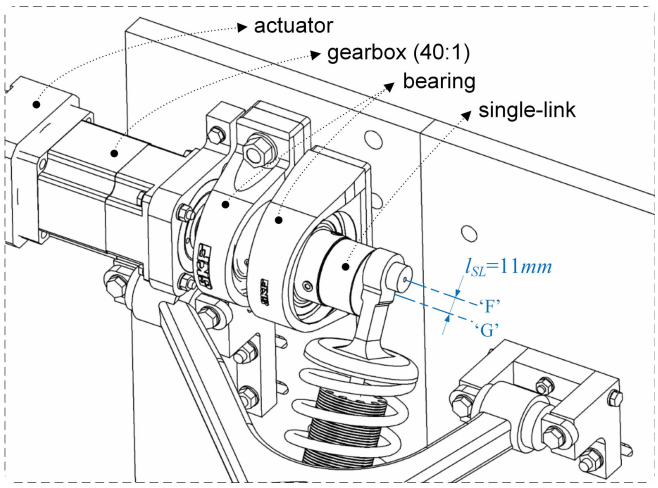

Fig. 6. Isometric view of the single-link transmission assembly in the SAVGS quarter-car test rig.

spring-damper unit. The two supporting bearings are attached onto the sprung mass, and they protect the gearbox output shaft from bending moments, with the axial torque (T_{SL}) applied only. The single-link implemented in this way has benefits of structural simplicity and high torsional stiffness [24].

C. Design of Excitation Mechanism

An excitation mechanism is added to enable road disturbance forcing on the wheel. Due to space constraints in the test rig, a cam-driven excitation device is developed to convert the rotary motion of a cam into translational motion of a road plate. As shown in Fig. 7, an eccentric cylinder, which is driven by a rotary actuator, acts as the cam. A roller follower, which is always in contact with the cam, is fixed underneath the road plate. This arrangement forms a rolling friction pair between the actuation and the load, and it facilitates heavy load operation. In addition, four linear bearings, together with linear rails, are mounted at each corner to guarantee pure vertical translational motion of the road plate.

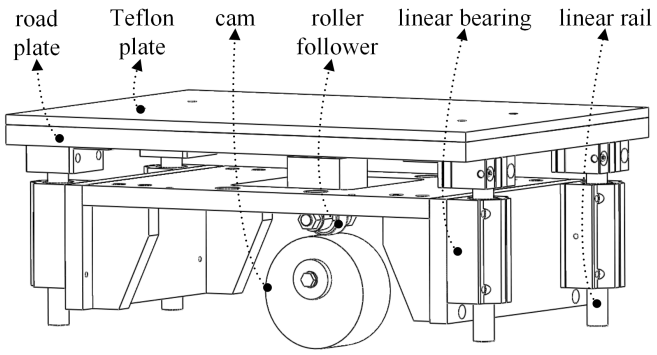

Fig. 7. Isometric view of the excitation mechanism in the SAVGS quarter-car test rig.

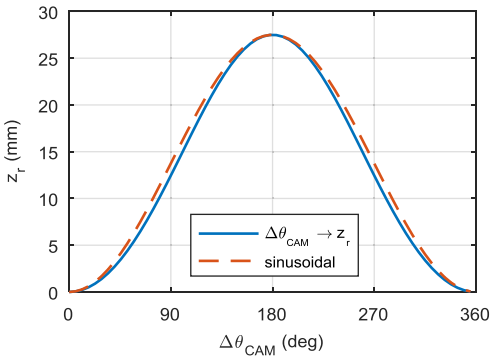

Fig. 8. Road profile generated by the eccentric cam and the roller follower mechanism. The solid line is the actual road height against the cam angle, while the dashed line is the approximated sinusoidal function for the generation of target road profiles.

The road height (z_r) variation against the cam angle can be derived through the geometric relationship between the cam and the roller follower, as shown by the solid line in Fig. 8. It is approximated by a sinusoidal function

$$z_r = \frac{h_{\mathrm{CAM}}}{2}(1 - \cos \Delta\theta_{\mathrm{CAM}}) \tag{5}$$

where h_{CAM} is the difference between the cam's tip radius and base radius.

The cam, together with its transmission and actuation assembly, is accommodated inside two parallel H-profile beams (as shown in Fig. 9). Due to this space constraint, a cam with $h_{\mathrm{CAM}} = 27.5$ mm is chosen. Inevitably this limits the maximum peak-to-peak road height that is reachable in the experimental study to 27.5 mm, which is deemed to be adequate for the present purposes.

D. Test Rig Implementation

With the critical mechanical parts discussed earlier, the SAVGS quarter-car test rig is set up, as shown in Fig. 9, H-profile beams constitute the supporting frame, making the whole test rig portable. The single link at the static and nominal equilibrium is illustrated, respectively, in Fig. 9(a) and (b). The cam and the roller follower in the road excitation mechanism are shown in Fig. 9(c).

In order to measure the system performance and to implement close-loop control, the following steps are taken.

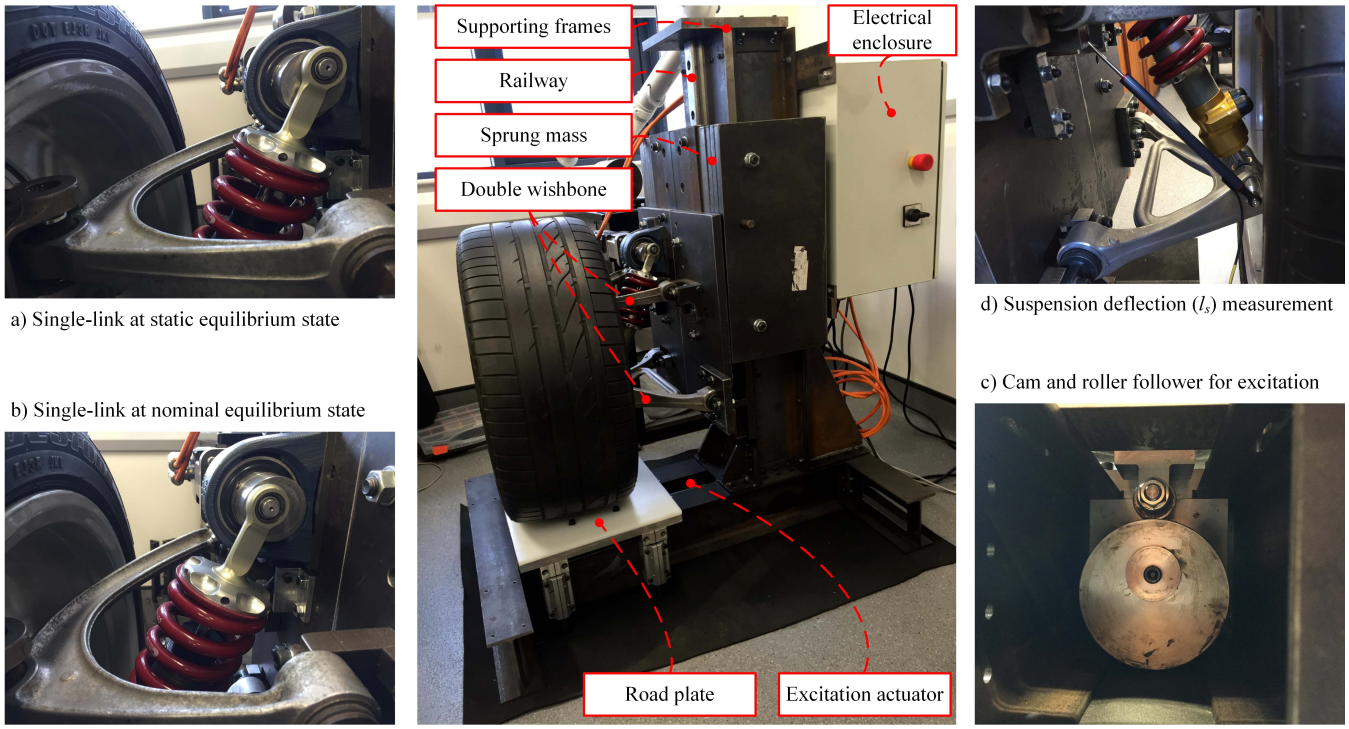

Fig. 9. Mechanical design and implementation of the SAVGS quarter-car test rig. It mainly comprises 1) cam-driven excitation mechanism, 2) double-wishbone suspension assembly, 3) single-link and its actuation assembly, and 4) sprung mass assembly with vertical translation only.

1) A uniaxial accelerometer is attached on the sprung mass to measure its vertical acceleration.
2) A linear potentiometer is mounted between the sprung mass and the spring-damper lower end eye to obtain the suspension deflection, as shown in Fig. 9(d).
3) Two permanent-magnet synchronous motors (PMSMs) are selected to drive the single link and the cam separately, with the actual position, velocity, and torque acquired by internal quadrature optical encoders and current sensors.
4) A real-time controller is adopted to communicate with an industrial computer (for the human-machine interaction), two PMSMs, and all the sensors mentioned earlier.

In summary, the features of the SAVGS quarter-car test rig are as follows.

1) All the mass properties are the same as an actual GT (Ferrari F430 real axle).
2) The suspension kinematics (e.g., the installation ratio) is considered, as an actual suspension assembly is utilized and reconstructed.
3) The target road profiles can be accurately generated through the motion control of the cam actuator.
4) Real-time control and monitoring of the embedded system is employed.
5) The test rig system enjoys structural simplicity and compactness.

III. Control Design and Implementation

This section specifies the SAVGS overall system control design and implementation, as shown in Fig. 10. First, an outer-loop H-infinity control is synthesized to enhance both the ride comfort and the road holding, with an equivalent linear model utilized. Second, an inner-loop actuator control is also developed to track the desired single-link velocity ($\omega_{\mathrm{SL}*}$), while ensuring that none of the actuator constraints (voltage, current, power, torque and speed) are violated. Finally, a mechatronic system of the SAVGS test rig is constructed for the overall control implementation, including the H-infinity control, the actuator speed tracking, and $\omega_{\mathrm{SL}*}$ and $\omega_{\mathrm{CAM}*}$, in the single-link and excitation mechanism, respectively.

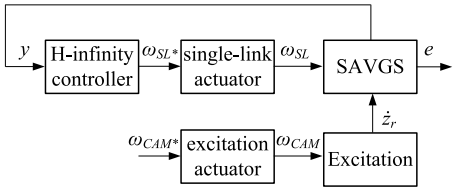

Fig. 10. Schematic of the SAVGS test rig system overall control. y corresponds to the system measurements, while e corresponds to the suspension performance objectives. ω_{SL} denotes the angular velocity of the sing-link while ω_{CAM} denotes that of the cam. $\dot{z}_r$ is the vertical road velocity.

A. Linear Equivalent Model

A linear model of the quarter-car test rig is necessary for H-infinity control synthesis. In previous studies of active suspensions, linear models with two pure vertical motions are widely applied, in which the geometric nonlinearity is not considered. In [12], a nonlinear model is first built and then linearized at a trim state of $\Delta\theta_{\mathrm{SL}} = 90^\circ$ to synthesize an H-infinity control for the SAVGS quarter car. However, the

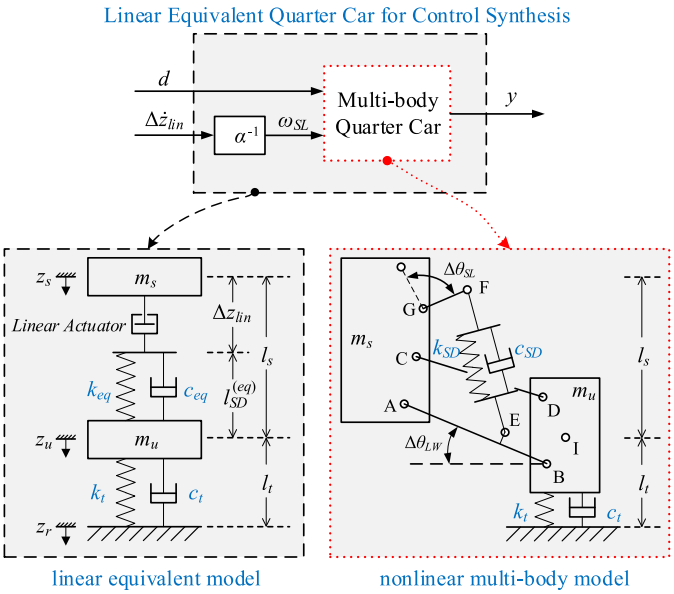

Fig. 11. Schematic of the linear equivalent modeling method. The dashed block is the equivalent model for linear control synthesis. The dotted block is the nonlinear multibody model. The function α converts the equivalent linear actuator velocity ($\dot{z}_{\text{lin}}$) to the rotary single-link velocity (ω_{SL}). d corresponds to the exogenous disturbance while y to the system measurements. (eq) denotes equivalent variables.

linear model obtained in this way is not accurate when a large single-link offset is required.

An equivalent modeling method, proposed in [10] and [11], is adopted for the SAVGS quarter-car test rig, as shown in Fig. 11. The equivalent model is purely linear, with the geometric nonlinearities associated with the single-link angle variation ($\Delta\theta_{\text{SL}}$) lumped into the function α.

The following assumptions are made to derive the linear equivalent model from a nonlinear multibody model of the system [24].

1) *Geometric Equivalence:* Both models have the same suspension deflection ($l_s = z_u - z_s$, the vertical distance between the sprung mass center and the unsprung mass center) and the same tire deflection ($l_t = z_r - z_u$, the vertical distance between the unsprung mass center and the road surface). The suspension deflection in the equivalent model is

$$l_s = \Delta z_{\text{lin}} + l_{\text{SD}}^{(\text{eq})} \tag{6}$$

where Δz_{lin} is the displacement increment of the linear actuator with respect to its nominal equilibrium state

$$\Delta z_{\text{lin}} = z_{\text{lin}} - z_{\text{lin}}^{(\text{ne})} \tag{7}$$

and $l_{\text{SD}}^{(\text{eq})}$ is the equivalent spring-damper length.

2) *Actuator Equivalence:* Both the actual rotary actuator and the equivalent linear actuator must have the same power output

$$T_{\text{SL}}\omega_{\text{SL}} = F_{\text{SD}}^{(\text{eq})}\dot{z}_{\text{lin}} \tag{8}$$

where $F_{\text{SD}}^{(\text{eq})}$ denotes the equivalent spring force.

3) *Spring-Damper Equivalence:* The equivalent spring needs to satisfy Hooke's law, while the equivalent damper has the same energy dissipation as the actual one

$$k_{\text{eq}} = \frac{dF_{\text{SD}}^{(\text{eq})}}{dl_{\text{SD}}^{(\text{eq})}}$$

$$c_{\text{eq}}\left(\frac{dl_{\text{SD}}^{(\text{eq})}}{dt}\right)^2 = c_{\text{SD}}\left(\frac{dl_{\text{SD}}}{dt}\right)^2 \tag{9}$$

where l_{SD} is the actual spring-damper length (the distance between points "E" and "F").

Coefficient functions, which are for the conversion from the multibody model to the equivalent one, are listed in (10). They are all dependent on the single-link angle ($\Delta\theta_{\text{SL}}$) and the lower wishbone angle ($\Delta\theta_{\text{LW}}$)

$$\begin{aligned}\alpha &= \alpha(\Delta\theta_{\text{SL}}, \Delta\theta_{\text{LW}}) = \dot{z}_{\text{lin}}/\omega_{\text{SL}}\\ \gamma_k &= k_{\text{eq}}(\Delta\theta_{\text{SL}}, \Delta\theta_{\text{LW}})/k_{\text{SD}}\\ \gamma_c &= c_{\text{eq}}(\Delta\theta_{\text{SL}}, \Delta\theta_{\text{LW}})/c_{\text{SD}}.\end{aligned} \tag{10}$$

Equation (10) can be derived from (6)–(9). The variation of each coefficient against $\Delta\theta_{\text{SL}}$ and $\Delta\theta_{\text{LW}}$ is shown in Figs. 12–14. Both k_{eq} and c_{eq} vary only marginally with $\Delta\theta_{\text{SL}}$ and $\Delta\theta_{\text{LW}}$, and are therefore approximated as constants by their value at the nominal state ($\gamma_k = 0.3806$, $\gamma_c = 0.3604$), in which the single-link offset is 90°, shown as the red marks in Figs. 12 and 13, respectively. The dependence of function α with the lower wishbone angle ($\Delta\theta_{\text{LW}}$) is small; therefore, it can be approximated by a parabolic equation with respect to the single-link angle ($\Delta\theta_{\text{SL}}$) only, as shown by the dashed line in Fig. 14.

The motion equations of the SAVGS linear equivalent model are listed in (11), with the mass of the equivalent linear actuator neglected due to the small inertia of the single link

$$\begin{aligned}m_s\ddot{z}_s &= k_{\text{eq}}(\Delta l_s - \Delta z_{\text{lin}}) + c_{\text{eq}}(\dot{l}_s - \dot{z}_{\text{lin}})\\ m_u\ddot{z}_u &= -k_{\text{eq}}(\Delta l_s - \Delta z_{\text{lin}}) - c_{\text{eq}}(\dot{l}_s - \dot{z}_{\text{lin}}) + k_t\Delta l_t + c_t\dot{l}_t.\end{aligned} \tag{11}$$

B. H-Infinity Control Synthesis

The H-infinity methodology is widely applied to linear multi-input multi-output systems due to its robustness. This control technique aims to minimize the disturbance propagation to the system performance objectives. The standard configuration of the H-infinity synthesis is illustrated in Fig. 15.

The H-infinity controller designed for the SAVGS quarter car in [10] and [11] is modified and adapted to the rig, as follows.

1) The exogenous disturbance in the rig is: $d = [d_1\ d_2]$. d_1 is an exogenous command signal of the linear equivalent actuator displacement, $\Delta z_{\text{lin}(e)}$, to enable zero or low frequencies (0–1 Hz) tracking, for example to set the nominal position of the single link ($\Delta\theta_{\text{SL}} = 90°$). d_2 is the vertical road velocity. The SAVGS has beens theoretically proven to be effective with both disturbance

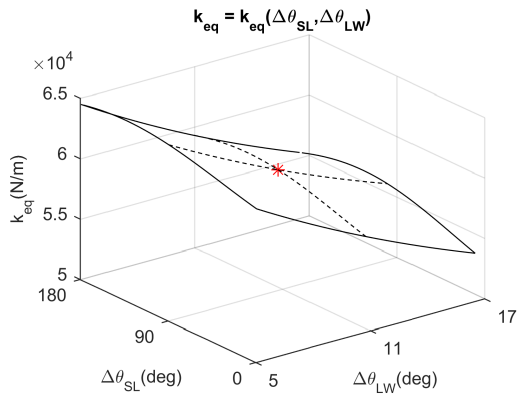

Fig. 12. Equivalent spring stiffness (k_{eq}) variation against the single-link angle ($\Delta\theta_{SL}$) and the lower wishbone angle ($\Delta\theta_{LW}$). Red mark ($*$) is k_{eq} at the nominal state.

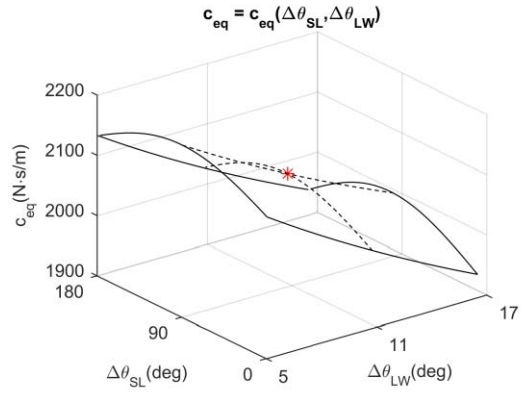

Fig. 13. Equivalent damping coefficient (c_{eq}) variation against the single-link angle ($\Delta\theta_{SL}$) and the lower wishbone angle ($\Delta\theta_{LW}$). Red mark ($*$) is c_{eq} at the nominal state.

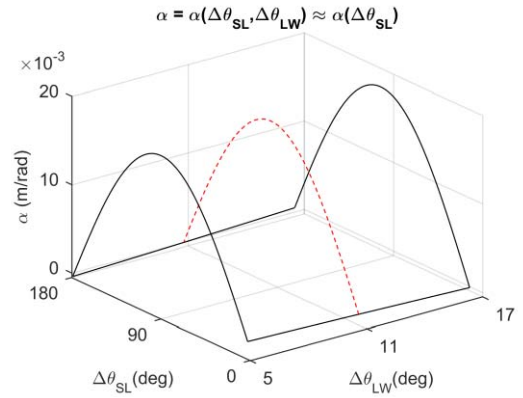

Fig. 14. Conversion function αagainst the single-link angle ($\Delta\theta_{SL}$) and the lower wishbone angle ($\Delta\theta_{LW}$). The dashed line is at the equilibrium value of the lower wishbone angle ($\Delta\theta_{LW}$).

of the vertical road velocity and the load transfer [10]. However, the latter is not included here, as it cannot be emulated by this quarter-car test rig.

2) The performance objectives to be minimized are $e = [e_1\ e_2\ e_3\ e_4]$. e_1 is the $\Delta z_{\text{lin}(e)}$ tracking error. e_2 and e_3 are the penalized sprung mass acceleration and tire deflection, respectively, both of which are the major objectives to evaluate ride comfort and road holding in a quarter-car. e_4 is the control effort, which is penalized to confine the single-link operation within a specified working frequency range (0–10 Hz), and also to reject the sensor noise to eliminate the output ripple of the actuator.

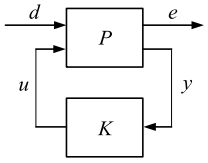

Fig. 15. Generalized regulator configuration of the H-infinity control application. P corresponds to a linear plant in state-space representation, K corresponds to the synthesized H-infinity controller, d corresponds to the exogenous disturbance, u corresponds to the manipulated variables, e corresponds to the performance objectives to be minimized, and y corresponds to the system measurements for feedback [27].

3) The measurements $y = [y_1\ y_2\ y_3]$ are selected given the feasibility of the sensors: y_1 is the suspension deflection measured by a linear potentiometer. y_2 is the vertical acceleration of the sprung mass, which is acquired through a uniaxial accelerometer. y_3 is the tracking error of the equivalent linear actuator displacement, which is obtained by an optical quadrature encoder in the single-link actuator.

4) The manipulated variable u is the command velocity of the linear equivalent actuator ($\dot{z}_{\text{lin}}$).

Weighting functions penalize the importance between multiple objectives at different frequency ranges, and they are also tuned to reject sensors noise, as follows.

1) In the case of the weighting functions of the exogenous disturbances [W_{road}, $W_{z\text{lin}}$], their dc values normalize the inputs with respect to their maximum values, taken as 0.25 m/s and 0.02 m, respectively, for the vertical road velocity ($\dot{z}_r$) and for the linear equivalent actuator displacement (Δz_{lin}). In addition, W_{zlin} incorporates a low-pass filter to avoid the conflict in the frequency domain between the exogenous command signal of $\Delta z_{\text{lin}(e)}$ (0–1 Hz) and the control output u (1–10 Hz)

$$W_{\text{road}} = 0.25, \quad W_{z\text{lin}} = 0.02\frac{1}{s/(2\pi \cdot 1) + 1}. \quad (12)$$

2) In the case of the weighting functions of the performance objectives [W_{err}, W_{Acc}, W_{TD}, W_{eff}], their cornering frequency is selected to match the desired frequency bandwidth of the active suspension, while their dc values can be tuned to be either conservative or aggressive. A second-order transfer function W_{eff} is applied to also reject the accelerometer noise (concentrates between 10 and 20 Hz), which results in the output torque ripple of the actuator and the single-link vibration

$$W_{\text{err}} = \frac{1}{0.004} \cdot \frac{\frac{s}{2\pi \cdot 120} + 1}{\frac{s}{2\pi \cdot 0.3} + 1}, \quad W_{\text{Acc}} = \frac{1}{3} \cdot \frac{1}{\frac{s}{2\pi \cdot 10} + 1}$$

$$W_{\text{TD}} = \frac{1}{0.005} \cdot \frac{1}{\frac{s}{2\pi \cdot 5} + 1}, \quad W_{\text{eff}} = \frac{1}{0.1} \cdot \frac{\left(\frac{s}{2\pi \cdot 10} + 1\right)^2}{\left(\frac{s}{2\pi \cdot 1000} + 1\right)^2}. \quad (13)$$

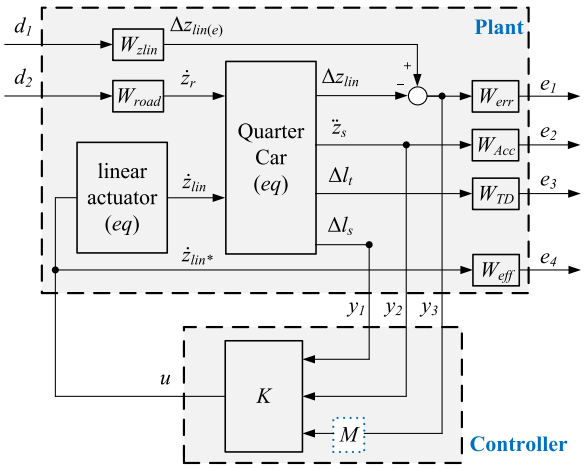

Fig. 16. H-infinity control synthesis with the linear equivalent model of the SAVGS quarter car [24]. Variables [d], [e], [y], and [u] correspond to those in Fig. 15. [W_{zlin} W_{road}] are disturbance weighting functions for the exogenous command of the linear equivalent actuator displacement ($\Delta z_{\text{lin}(e)}$) and the vertical road velocity ($\dot{z}_r$), respectively. [W_{err} W_{Acc} W_{TD} W_{eff}] are the objective weighting functions for the exogenous command tracking error, the sprung mass vertical acceleration, the tire deflection and the control effort, respectively. Block "K" is the synthesized H-infinity controller. Block "M" is subsequently added to zero the exogenous command tracking error "y_3."

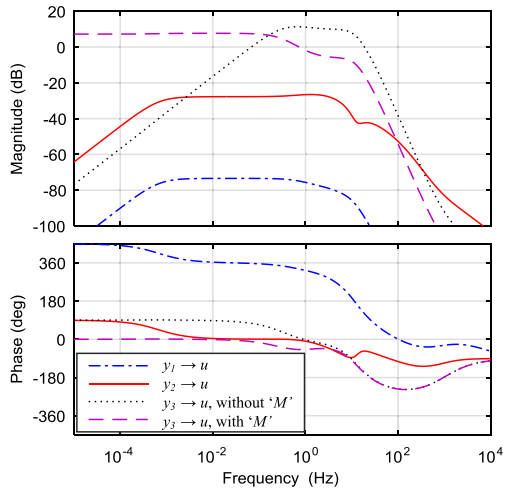

Fig. 17. Bode magnitude diagrams of the synthesized controller. [y_1 y_2 y_3], [u], and "M" correspond to those in Fig. 16.

A first-order transfer function (with the cutoff frequency assumed to be 17.8 Hz [11]) is adopted to approximate the limited bandwidth of the actuator frequency response behavior.

With the identified input and output variables and the tuned weighting functions, the configuration scheme for H-infinity control synthesis is shown in Fig. 16.

The "Quarter car (eq)" is the linear equivalent model in state-space representation. The constructed plant (top dashed block in Fig. 16) corresponds to "P" in Fig. 15. By means of the MATLAB command *hinfsyn*, an H-infinity controller "K" is synthesized. The transfer function "M" filtering the output y_3 has a free integrator and aims to ensure a zero steady-state tracking error of the exogenous command ($\Delta z_{\text{lin}(e)}$) [11], [27]. In order to facilitate simple tuning of the desired tracking response characteristics in the time domain (e.g., rise

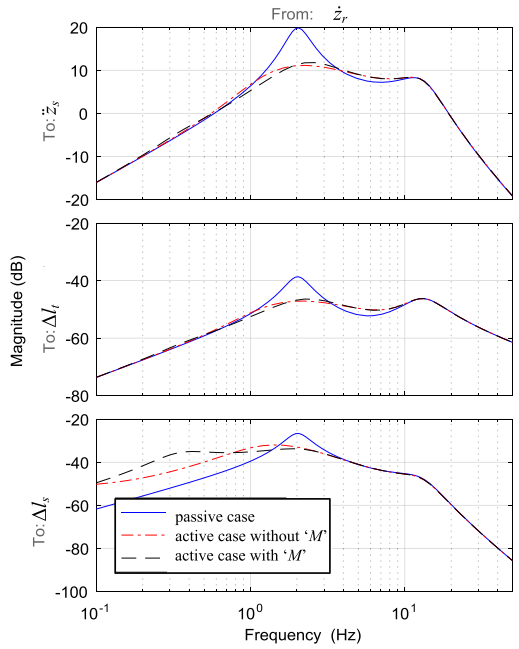

Fig. 18. Bode magnitude diagrams of the linear equivalent SAVGS quarter-car model: from vertical road velocity to sprung mass vertical acceleration (top), tire deflection (middle), and suspension deflection (bottom).

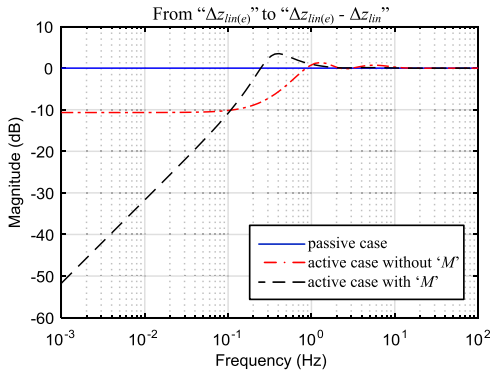

Fig. 19. Bode magnitude diagrams of the linear equivalent SAVGS quarter-car model: from the normalized exogenous command of the linear equivalent actuator displacement ($\Delta z_{\text{lin}(e)}$) to its tracking error ($\Delta z_{\text{lin}(e)}$−Δz_{lin}).

time) by experiments, "M" is added and tuned *a posteriori*, and it is not part of the H-infinity synthesis. The overall controller (bottom dashed block in Fig. 16) includes both the synthesized "K" and the experimentally tuned "M," which is given by

$$M = \frac{s/(2\pi \cdot 1) + 1}{s}. \tag{14}$$

Theoretical analysis with the linear equivalent model is performed: bode diagrams of the overall controller without "M" and with "M" are shown in Fig. 17. It can be seen that the sole controller "K" is a bandpass filter for all inputs. The path from "y_3" to "u" is changed to a low-pass filter due to block "M," as it takes effect at low frequencies to zero the $\Delta z_{\text{lin}(e)}$ tracking error.

Bode magnitude diagrams of the linear equivalent model in passive (i.e., Δz_{lin} is fixed at the value of 0) and active cases are shown in Figs. 18 and 19. The synthesized controller

significantly improves the suspension performance, as the objective gains are attenuated (by 6–8 dB) at around the human-sensitive frequency of 2 Hz. The addition of "M" slightly affects the frequency response of the sprung mass acceleration and tire deflection, and it only increases the suspension deflection gain below 1 Hz, as the actuator takes effect to track the linear actuator reference displacement ($\Delta z_{\text{lin}(e)}$) at low frequencies (also shown in Fig. 19).

Overall, the addition of the transfer function "M" benefits the zero tracking error of the exogenous command, without affecting the closed-loop system performance. Therefore, "M" included in the final design.

The linear analysis in this section gives an indication of the expected SAVGS performance improvement over the passive suspension. Further and more accurate demonstration of the dynamic performance improvement is provided later by nonlinear simulations and experiments in Sections IV and V.

C. Single-Link Actuator Modeling and Control

A PMSM (also known as brushless AC motor) is selected as the single-link actuator due to its high power density, high efficiency, and fast response. The classical "d–q" vector modeling and control algorithm (also referred to as field-oriented control) is commonly adopted in ac motors [28], [29]. The basic idea is to transform three-phase stator current into two independent variables: a magnetic field-generating part (i_d) and a torque-generating part (i_q). The electrical dynamics of this equivalent d–q model are written as

$$\begin{aligned}\frac{di_d}{dt} &= \frac{1}{L_s}(v_d - R_s i_d + \omega_e \psi_q)\\ \frac{di_q}{dt} &= \frac{1}{L_s}(v_q - R_s i_q - \omega_e \psi_d)\end{aligned} \tag{15}$$

where L_s and R_s are the d–q phase resistance and inductance, v_d and v_q are the voltages in the d-axis and q-axis, respectively. $\psi_d = L_s i_d + \psi_a$ and $\psi_q = L_s i_q$ are the flux linkages in d–q reference frames, ψ_a is the flux linkage of the rotor permanent magnet, and ω_e is the electrical frequency. The output electromagnetic torque (T_{em}) of the PMSM is then given by

$$T_{\text{em}} = 1.5 n_{\text{pp}}(i_q \psi_d - i_d \psi_q) \tag{16}$$

where n_{pp} is the number of the pole pairs.

The PMSM torque control is based on the widely utilized "zero d-axis current control" strategy, in which i_d is forced to be zero to ensure maximum torque-per-amp operation [30]. Equation (16) can be further written as

$$T_{\text{em}} = (1.5 n_{\text{pp}} \psi_a) \cdot i_q. \tag{17}$$

As both n_{pp} and ψ_a are constant values for a specific PMSM, the actuator torqueT_{em} is directly proportional with the q-axis current i_q. Therefore, the PMSM actuator can be simplified as a dc equivalent motor [30].

A cascaded velocity-current control scheme is performed for the single-link motion control, as shown in Fig. 20. The actuator velocity ω_{SL} is acquired through an optical quadrature encoder, and the actual current signals i_d and i_q are obtained by transforming measurements of the phase currents i_a, i_b, and i_c.

In the velocity loop, an acceleration feed-forward path is added in parallel with a proportional-integral controller to contribute to the reference signal tracking without further increasing the proportional gain. Moreover, velocity and acceleration/deceleration clamps are in place for safety. A first-order low-pass filter is applied to reduce the torque ripple and resonances from the motor and gearbox.

In the current loop, according to the "zero d-axis current control" strategy, the reference d-axis current i_{d*} is forced to zero, while a proportional-integral controller is applied to the i_{q*} tracking. The output voltages v_{d*} and v_{d*} are converted into three-phase ac voltage v_{a*}, v_{b*}, and v_{c*} (by means of the d–q inverse transformation) before feeding the inverter in the PMSM servo drive. In addition, a current clamp (0/+7.5 A) is added to limit the magnitude of the actuator high-speed shaft output torque and also to prevent the same torque from ever becoming negative thus avoiding the gearbox backlash effect. The power of the single-link actuator is intentionally limited to 500 W, which is a reasonable value for the SAVGS full-car application in terms of the actuator size and weight.

The main parameters of the single-link actuator and of the tuned controllers are listed in Table III in the Appendix.

Another PMSM (with a rated power of 3610 W and a rated torque of 9.85 N · m) is selected to drive the excitation mechanism with the same cascaded control scheme applied.

D. Control Implementation in Nonlinear System

The H-infinity control and the single-link actuator control are presented in Sections III-B and III-C, respectively, and they are further developed to adapt to the nonlinear mechatronic system of the SAVGS quarter-car test rig, as shown in Fig. 21.

1) The H-infinity control provides the reference velocity of the equivalent linear actuator ($\dot{z}_{\text{lin}*}$), which is converted into the single-link reference velocity ($\omega_{\text{SL}*}$) by function $\alpha = \dot{z}_{\text{lin}}/\omega_{\text{SL}}$. The actual single-link position ($\Delta\theta_{\text{SL}}$) is converted into the displacement of the equivalent linear actuator (Δz_{lin}) by function $\beta = \Delta z_{\text{lin}}(\Delta\theta_{\text{SL}})$, for utilization by the H-infinity controller.
   Functions α and β are shown in Fig. 22, where α is the parabolic approximation shown in Fig. 14 and β is the integral of α with respect to the single-link angle ($\Delta\theta_{\text{SL}}$).
2) The exogenous command of the equivalent linear actuator displacement ($\Delta z_{\text{lin}(e)}$) is fixed at the value of its nominal equilibrium state (corresponding to $\Delta\theta_{\text{SL}} = 90°$), where the single link has the maximum control influence [11].
3) The controllers are designed in continuous time but are subsequently discretized, due to the fact that the test rig physical controller, NI cRIO-9022 [33], has 200 Hz I/O sampling frequency. The discretization is implemented by MATLAB command *c2d* (*sys*, *0.005*, "*zoh*"), 5 ms is the sampling period.

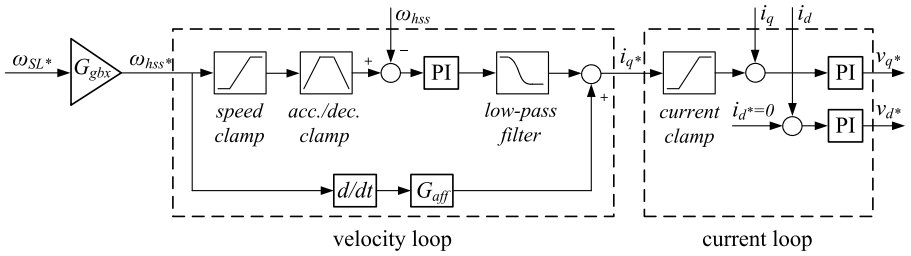

Fig. 20. Cascaded control scheme for the single-link actuator [32]. G_{gbx} (=40) is the single-link gearbox ratio. ω_{hss} is the high-speed shaft velocity of the actuator, while ω_{SL} is the velocity of the single-link, which is connected to the low-speed shaft of the actuator. G_{aff} is the feed-forward gain in the velocity control loop.

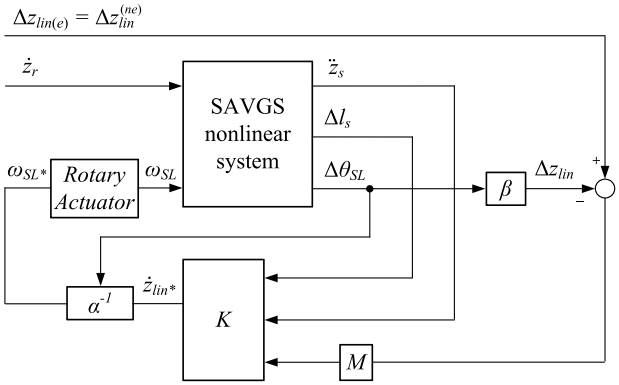

Fig. 21. Control application to the SAVGS nonlinear system. Blocks "K" and "M" correspond to those in Fig. 16. Functions α and β convert variables from the multibody model to the linear equivalent model. The exogenous command of the equivalent linear actuator displacement ($\Delta z_{\text{lin}(e)}$) is fixed at the value of its nominal equilibrium state.

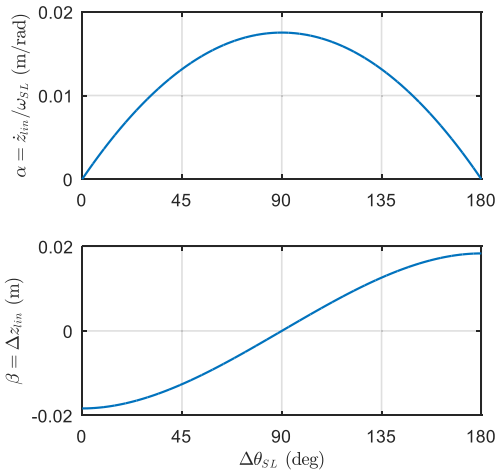

Fig. 22. Plots of functions α and β for conversion between the multibody and linear equivalent models.

Sections III-A to III-D theoretically complete the overall control design and implementation of the SAVGS quarter-car test rig, while the practical application is based on the test rig mechatronic system, which is constructed as follows.

E. Test Rig Mechatronic System

The electrical configuration and the software deployment are illustrated in Fig. 23. A physical controller (NI cRIO-9022) is acting as the core in this system. It is equipped with a real-time microprocessor, an FPGA module, I/O modules, and Ethernet modules [33]. This controller coordinates the electrical hardware of the following:

1) a servo drive (Kollmorgen S300) for the single-link actuator;
2) a servo drive for the excitation actuator (Kollmorgen AKD EtherCAT);
3) sensors of a uniaxial accelerometer and a linear potentiometer;
4) a PC.

The single-link actuator and its servo drive are utilized to convert the command velocity ($\omega_{\text{SL}*}$, from an analog output of the physical controller and fed into an analog input of the servo drive) to the actual one (ω_{SL}). As shown in Fig. 23 (middle dashed block), this actuator is a PMSM powered and controlled as follows. First, a rectifier converts the ac mains to a dc voltage (=320 V), and it feeds the dc bus in a pulse width modulation inverter. Second, the space vector modulation technique is adopted in the inverter to generate three-phase sinusoidal voltage (v_a, v_b, v_c) for the ac machine, with their reference signal (v_{a*}, v_{b*}, v_{c*}) given by the torque loop in the actuator controllers. It is worth noting that the ac mains power supply and the rectifier are only relevant to the test rig, whereas a dc battery and a low-to-high voltage dc–dc converter are to be employed on a real car instead [8].

The excitation actuator is also a PMSM with a similar working principle as the one for the single link. As shown in the bottom dashed block of Fig. 23, this actuator aims to convert the road profile reference signal ($\omega_{\text{CAM}*}$, $\theta_{\text{CAM}*}$) to the actual cam angle/velocity (ω_{CAM}, θ_{CAM}). By using an advanced EtherCAT servo drive, this excitation actuator can communicate with the physical controller (NI cRIO-9022) through the EtherCAT protocol. In this way both of the input ($\omega_{\text{CAM}*}$, $\theta_{\text{CAM}*}$) and output (T_{CAM}, ω_{CAM}, θ_{CAM}) signals can be digitally transmitted with reduced signal noise.

LabVIEW software is utilized to develop an embedded control and monitoring platform.

LabVIEW Program #1 is deployed in the real-time microprocessor (NI cRIO-9022), where critical control algorithms and communication protocols are mainly implemented, including the following:

1) the discrete H-infinity control;
2) the velocity loop control for the excitation actuator;

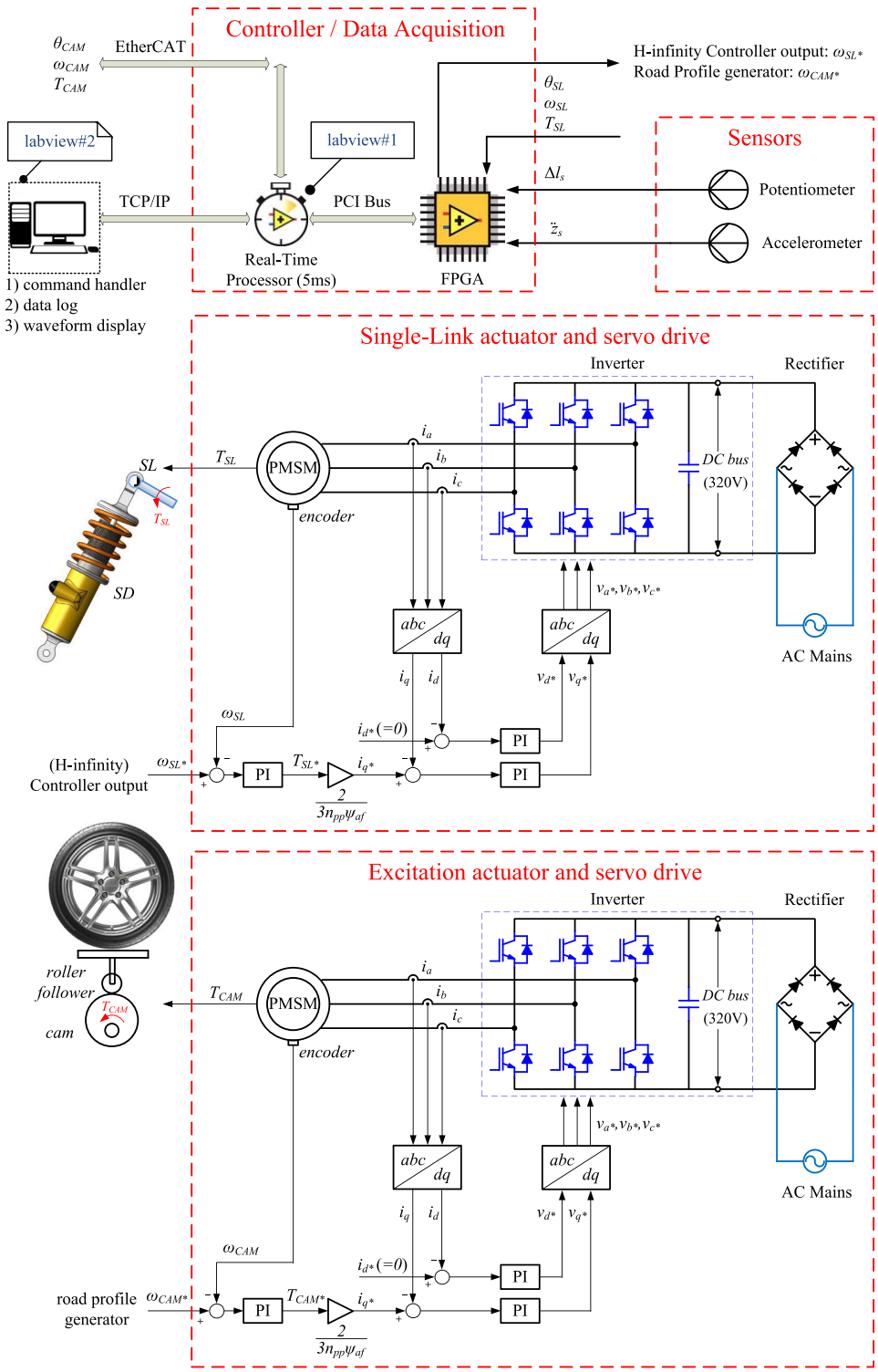

Fig. 23. Electrical implementation and the software deployment in the mechatronic system of the SAVGS quarter-car test rig

3) the communication with the FPGA module (access to I/O modules for data acquisition);
4) the communication with a PC by means of network protocols.

LabVIEW Program #2 is deployed in the industrial PC for the human–machine interaction. This program includes as follows:

1) command handlers (e.g., motor initialization/stop and passive/active switch);
2) waveform display (for the monitoring of all variables of interest);
3) data logging (e.g., the sprung mass acceleration and the suspension deflection);
4) further signal analysis based on historical records.

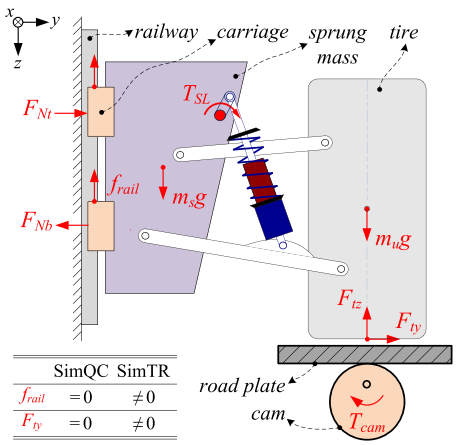

Fig. 24. Schematic of the nonlinear model of the SAVGS quarter-car test rig.

Compared to LabVIEW Program #1, tasks in Program #2 have lower priority and are less required in real time. However, functions such as data logging and waveform display consume larger memory space. Therefore, these tasks are split from the real-time processor and deployed in the PC. The benefits in this way are that: 1) the memory in the real-time microcontroller is released and 2) the deterministic loops and iterations (with a fixed execution period of 0.005 s) in the critical controllers (the outer-loop H-infinity control and the inner-loop velocity tracking) are guaranteed.

IV. Nonlinear Simulation and Analysis

With the mechanical structure, the electrical configuration and the control strategies discussed in Sections II and III, simulations with the nonlinear SAVGS system are performed in this section to theoretically analyze the test rig behavior.

A theoretical nonlinear quarter-car model with the actual rig parameters (referred to as "SimQC") is first built to explore the SAVGS potential in enhancing the suspension performance. In order to bridge the gap between the simulation results of the theoretical model and the experimental results of the actual test rig, practical features (e.g., the railway-sprung mass friction) existing in the rig are further included to construct a more realistic model (referred to as "SimTR").

A. Nonlinear Modeling of Quarter-Car and Test Rig

The SimQC includes the following nonlinearities [6]: 1) the kinematics of the multibody suspension assembly; 2) the nonlinear damping force characteristics; and 3) the electrical behavior (e.g., the saturations of the power, voltage, current, position, speed, and torque) of the single-link actuator.

In addition to these nonlinearities, the SimTR model (as shown in Fig. 24) includes the practical features existing in the rig: 1) the sprung mass-rail way friction f_{rail} and the wheel tire-road plate frictionF_{ty}; 2) the sensors noise in the potentiometer and the accelerometer measurements; and 3) the system discreteness from 200-Hz sampling frequency in the controllers' I/O ports [33].

f_{rail} and F_{ty} in the SimTR model have been identified through experimental results in the frequency domain, and approximated as follows [24]:

$$f_{\text{rail}} = \mu_r(|F_{\text{Nt}}| + |F_{\text{Nb}}|) \tag{18}$$

where F_{Nt} and F_{Nb} are the lateral load, respectively, acting on the top and the bottom carriage from the railway, μ_r (=0.03) is the friction coefficient between the railway and the carriages

$$F_{ty} = \min\left(1, \frac{|\dot{y}_H|}{\dot{y}_{H\text{th}}}\right) \times \mu_t |F_{\text{tz}}| \tag{19}$$

where $\dot{y}_H$ is the lateral velocity of the tire contact point with the road plate (point "H" in Fig. 1), $\dot{y}_{H\text{th}}$ (=0.05 m/s) is a shaping constant, and μ_t (=0.25) is the friction coefficient between the tire and the Teflon road plate.

The following Sections IV-B to IV-D present nonlinear simulation results with three typical road profiles.

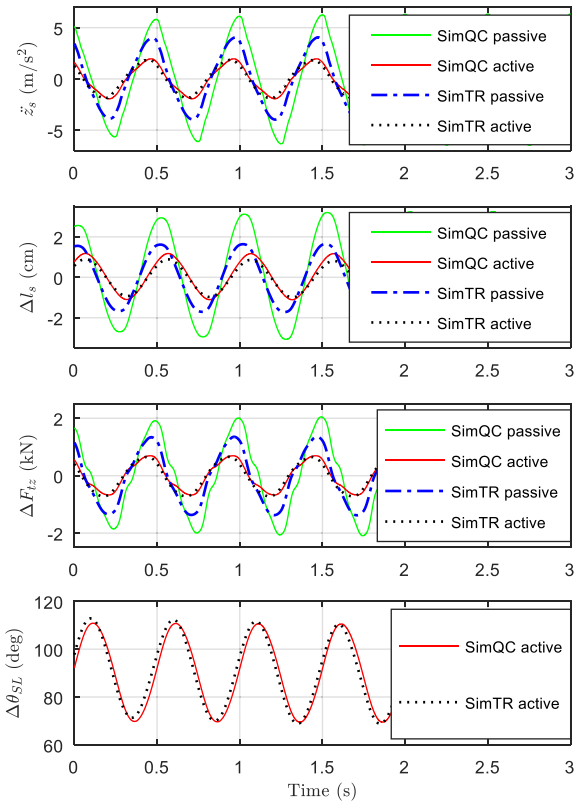

Fig. 25. Nonlinear simulation over harmonic road, with 2-Hz frequency, and 2.75-cm peak-to-peak amplitude. The variables depicted are (top-to-bottom): sprung mass acceleration, suspension deflection, tire force, and single-link angle.

B. Simulation With Harmonic Road

The frequency at around 2 Hz is thought to be human sensitive [34]. Fig. 25 shows the time response over a sinusoidal road disturbance, with 2-Hz frequency and 2.75-cm peak-to-peak amplitude.

The comparison between "SimQC passive" and "SimQC active" shows that the SAVGS can significantly attenuate the performance objectives, with a 67%, 63%, and 64% (rms) drop in the sprung mass acceleration, the suspension deflection, and the vertical tire force, respectively. On the other hand, the comparison between "SimQC passive" and "SimTR passive"

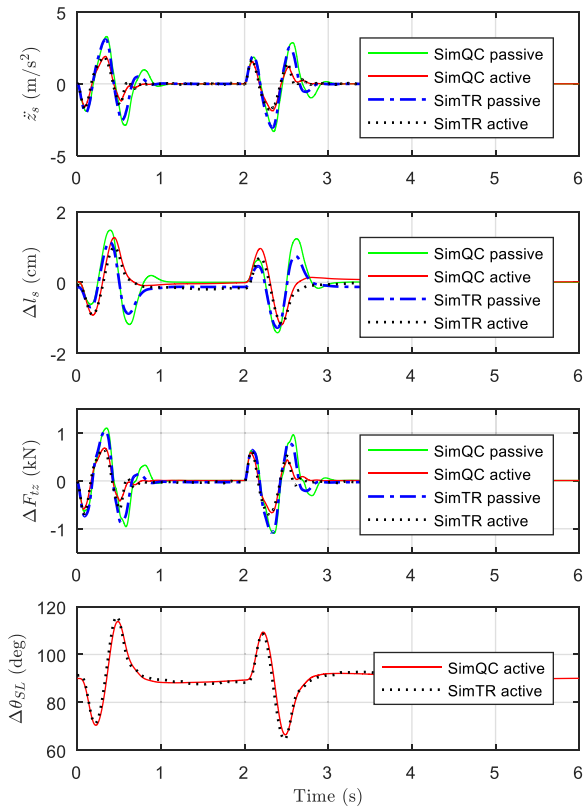

Fig. 26. Nonlinear simulation over a smoothed bump (0–2 s) and hole (2–4 s), with 2.75-cm peak-to-peak amplitude in road height, 1.4-m width, and 10 km/h driving speed in both cases. The variables depicted are (top to bottom): sprung mass acceleration, suspension deflection, tire force, and single-link angle.

shows the dynamics attenuation caused by the sprung mass-railway friction (f_{rail}), while the robust controller is able to maintain "SimQC active" and "SimTR active" nearly identical.

C. Simulation With Smoothed Bump and Hole

A bump is a vertical road deflection commonly utilized to slow motor-vehicle traffic in order to improve safety conditions, while a hole is a structural failure.

Nonlinear simulation is performed over a smoothed bump and hole, both of which can be approximated by sinusoidal functions. The road height difference, 2.75 cm, is constrained by the profile of the utilized cam. The simulation emulates the case of a car traveling at a speed of 10 km/h and running over a smoothed bump/hole with 1.4-m width, respectively, at 0 and 2 s (the parameters selected here concern the rated torque-speed envelope of the excitation actuator). The results are shown in Fig. 26.

The comparison between "SimQC passive" and "SimQC active" shows once again the performance improvement by the SAVGS: the sprung mass acceleration, the suspension deflection, and the tire force drop by 47%, 21%, and 42% (rms), respectively, for the bump case, and 47%, 23%, and 43% (rms) when the car experiences the hole. Further comparison between "SimQC passive" and "SimTR passive" also shows the dynamics attenuation by the rig railway friction. Despite the experimental uncertainties (e.g., the friction, the sensor noise, and the controller discreteness), "SimTR active" still matches "SimQC active" due to the controller robustness.

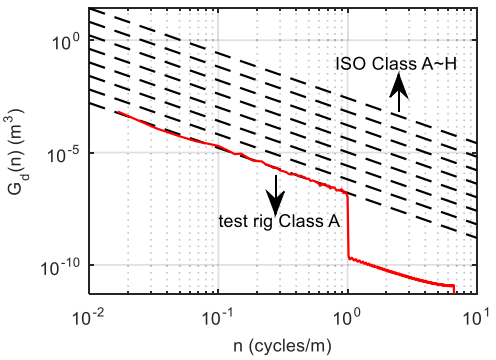

Fig. 27. PSD estimate of the ISO random road (dashed lines) and the one generated by the cam-driven excitation mechanism (solid red line).

D. Simulation With Random Road

The random road is generated according to [35], where the road profile is described in the form of power spectral density (PSD)

$$G_d(n) = G_d(n_0)\left(\frac{n}{n_0}\right)^{-\omega}$$
$$G_d(n_0) = 10^{-6}\cdot 2^{2k} \tag{20}$$

where variable n is the spatial frequency (cycles per meter), n_0 and ω are constants while $k = 2$–9 corresponds to road Classes A–H, which reflect the roughness of the road surface (dashed parallel lines shown in Fig. 27). The spatial frequency range $[n_{\min}, n_{\max}]$ is recommend as [0.01, 10] for the general on-road vehicles.

The random road profile in the time domain is generated with the equations as follows [11]:

$$h(x = Vt) = \sum_{n_i = n_{\min}}^{n_{\max}} A_i \cos(2\pi n_i V t + \phi_i)$$
$$\frac{A_i^2/2}{\Delta n} = G_d(n)|_{n=n_i} \tag{21}$$

where A_i is the amplitude corresponding to the spatial frequency n_i, while ϕ_i is a random number distributed in the interval $[0,\ 2\pi]$. The emulated driving speed V and the spatial frequency range $[n_{\min}, n_{\max}]$ are reconsidered with the following experimental limitations taken into account: 1) the sampling frequency of the physical controllers in the rig is 200 Hz [33]; thus, the maximum frequency in the generated road profile should be below 100 Hz and 2) the position/velocity control loop in the excitation actuator has a bandwidth of 0–75 Hz [32]. Given these two limitations, the parameters of the random road profile for both nonlinear simulation and experimental study are selected as: the vehicle driving speed $V = 60$ km/h, the spatial frequency range $[n_{\min}, n_{\max}] = [0.01,\ 1]$ cycles/m, the road length $L = 1$ km, and the spatial frequency step $\Delta n = 0.001$ cycles/m ($\Delta n \le 1/L$ should be satisfied). In addition, the actual test rig can only deal with Class A due to the constraints of the cam radius and the rig space.

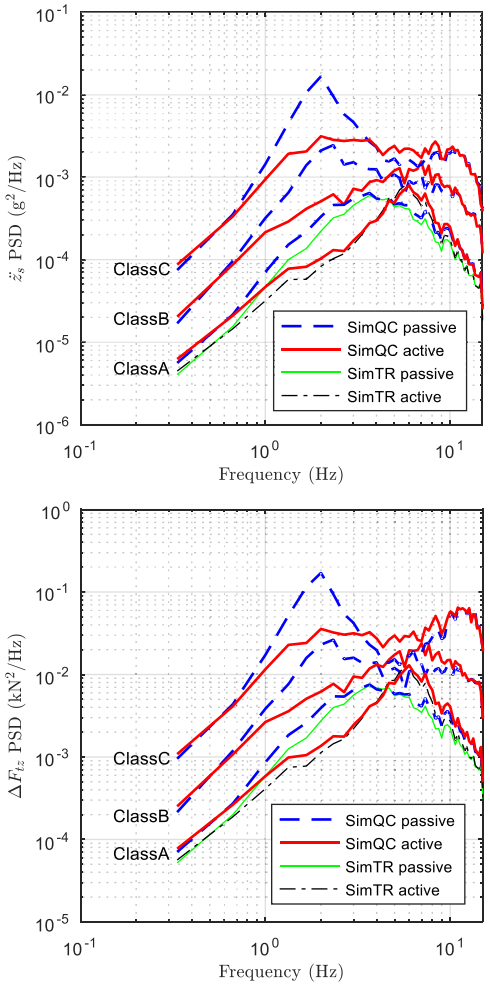

Fig. 28. Nonlinear simulation over random road (Classes A–C): the PSD estimate of the sprung mass acceleration (top) and the vertical tire force (bottom).

The PSD estimate of the modified Class A road profile for nonlinear simulations as well as experimental study is shown as the solid line in Fig. 27.

The nonlinear simulation PSDs of the sprung mass acceleration and the vertical tire force are shown in Fig. 28. The comparison between "SimQC passive" and "SimQC active" shows the potential in the performance enhancement by the SAVGS, as the objective gains (the sprung mass vertical acceleration and the tire force) at around the human-sensitive frequency (1–3 Hz) are appreciably attenuated. The comparison between "SimQC" and "SimTR" indicates that the influence of the railway friction is overall slight, as it can either attenuate or intensify the sprung mass vibration with irregular road profiles.

V. Experiments and Discussion

In this section, experiments with the SAVGS quarter-car test rig are performed to evaluate the practical feasibility (with the ride comfort mainly considered) and the accuracy of the modeling assumptions. The same road profiles discussed in Section IV are tested to compare directly with the nonlinear simulation results.

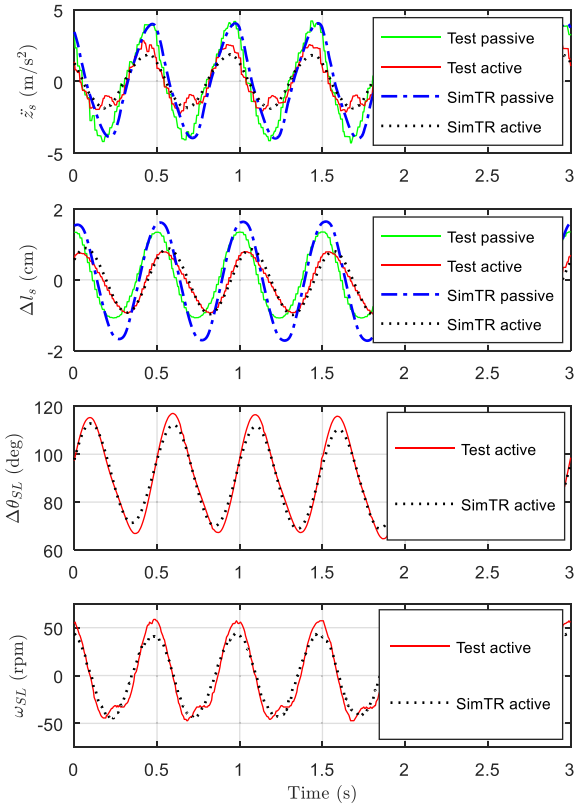

Fig. 29. Test results over a harmonic road profile, with 2-Hz frequency, and 2.75-cm peak-to-peak amplitude [24]. The variables depicted are (top to bottom): sprung mass acceleration, suspension deflection, single-link angle, and single-link velocity.

A. Tests With Harmonic Road

Test results over a 2-Hz harmonic road profile are shown in Fig. 29. The comparison between "Test passive" and "Test active" shows notable performance improvement of the SAVGS, as the sprung mass vertical acceleration and the suspension deflection decrease by 41% and 31% (rms), respectively [24]. The comparison between "Test" and "SimTR" suggests that the accuracy of the nonlinear models, as the response in both the passive and active cases are matched, despite the largest discrepancy in the suspension deflection.

B. Tests With Smoothed Bump and Hole

Test results over a smoothed bump and hole are shown in Fig. 30. The comparison between "Test passive" and "Test active" shows that the SAVGS can practically enhance the suspension performance, with 33% drop in the sprung mass vertical acceleration at the bump and 38% at the hole. The comparison between "Test" and "SimTR" shows that the model developed is accurate. However, the largest discrepancy occurs in the suspension deflection, which can settle at different levels (see the Δl_s for the "Test active" case in Fig. 30) as a result of the tire's lateral deformation, the tire-road plate static friction, and the sprung mass-railway static friction. By further observing the single-link angle ($\Delta\theta_{\mathrm{SL}}$ in Fig. 30), it can be seen that the SAVGS controller is capable of tracking the exogenous command of the equivalent

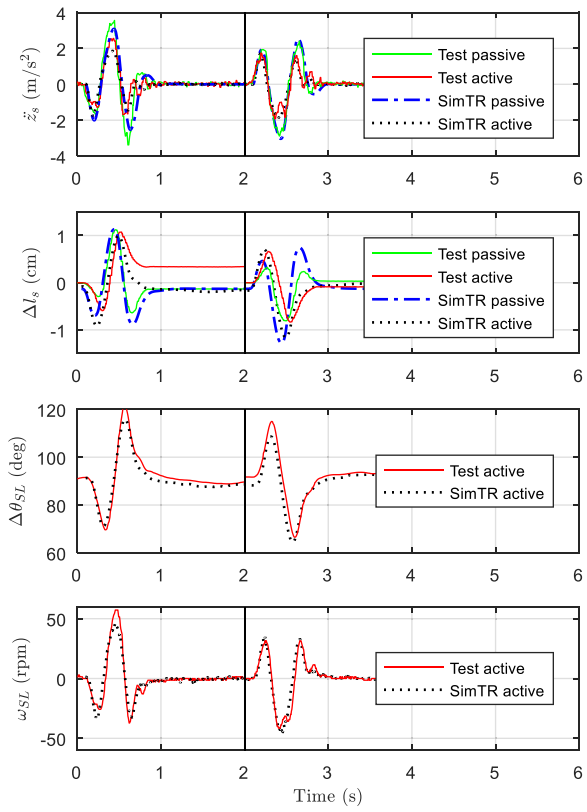

Fig. 30. Test results over a smoothed bump (0–2 s) and hole (2–4 s), with 2.75-cm peak-to-peak amplitude in road height, 1.4-m width, and 10 km/h driving speed. The variables depicted are (top to bottom): sprung mass acceleration, suspension deflection, single-link angle, and single-link velocity.

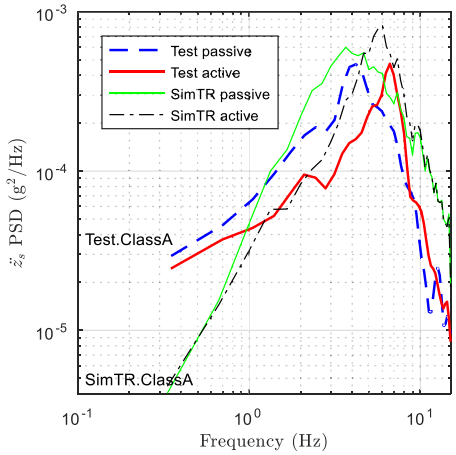

Fig. 31. Test results over the Class-A random road (the road profile applied is shown in Fig. 27): the PSD estimate for the sprung mass vertical acceleration.

linear actuator displacement ($\Delta z_{\text{lin}(e)}$, set at the value of its nominal state), as the single-link angle returns at 90° when the road disturbance ends.

C. Tests With Class A Random Road

The test results over the Class A random road (PSD estimate of which is shown as the solid red line in Fig. 27) are shown in Fig. 31. The comparison between "Test passive" and "Test active" shows that the SAVGS can improve the ride comfort even under a small road disturbance, as the sprung mass vertical acceleration is reduced at around human-sensitive frequency (1–3 Hz). The SAVGS performance marginally deteriorates at around 6–7 Hz, which can be tolerated especially with worse road profiles (e.g., Classes B and C, with simulation results presented in Fig. 28).

The comparison between "Test" and "SimTR" shows that they have similar profiles in the frequency domain. Due to the fact that the Class A random road has a small road disturbance input, the influence of the experimental uncertainties on the sprung mass acceleration is relatively significant, including: 1) sensors and environment noise; 2) the complexity introduced by friction (e.g., the tire-road plate friction); and 3) the complexity of the tire's lateral deformation, and so on.

VI. Conclusion

A quarter-car experimental study of the SAVGS is performed in this paper. A test rig of a GT double-wishbone suspension is designed, with an active single-link variant and a road excitation mechanism implemented. A linear equivalent modeling method is adopted to synthesize an H-infinity control scheme, with the geometric nonlinearity compensated. The designed controller actively adjusts the single-link velocity at higher frequencies to improve the suspension performance, or it stabilizes the single-link position at low frequencies by tracking an exogenous command.

The SAVGS (outer-loop) H-infinity control as well as the (inner-loop) single-link actuator control is further modified and adapted to the experimental test rig application.

The simulation results with a theoretical nonlinear quarter-car model indicate the potential of the SAVGS in improving both the ride comfort and the road holding. The practical features (e.g., the rig friction) existing in the rig are further considered and included in a nonlinear test rig model. This more realistic model compensates the testing behavior difference with the theoretical one, and also indicates the influence of the practical features on the experimental demonstration.

The experimental results with a sinusoidal road, a smoothed bump and hole, and a random road profile show that the following.

1) The SAVGS is practically feasible in both the mechanical implementation and the control application, as it significantly contributes to the ride comfort enhancement.
2) The SAVGS overall control is robust, as it is capable of dealing with the rig friction, the sensors noise and other experimental uncertainties.
3) The mathematical assumptions of the model are essentially correct, despite the complexity in the tire deformation and the rig friction.

The demonstrated feasibility of the SAVGS to improve suspension performance and the development of suitable control strategies open new avenues for the exploitation of this solution in the automotive sector.

TABLE I
MAIN PARAMETERS IN SAVGS QUARTER-CAR TEST RIG

Parameters	*Symbol*	*Value*	*Unit*
Weight of sprung mass	m_s	320	kg
Weight of unsprung mass	m_u	49	kg
Spring stiffness	k_{sd}	157614	N/m
Linearized damping	c_{sd}	5792	N/(m/s)
Tire's radial stiffness	k_t	275000	N/m
Tire's radial damping	c_t	300	N/(m/s)
Single-link length	l_{SL}	11	mm
Peak-to-peak road height	h_{CAM}	27.5	mm

TABLE II
NOMINAL GEOMETRIC PARAMETERS OF FERRARI F430 REAR SUSPENSION

Parameters	*Symbol*	*Value*	*Unit*
Height of roll centre	l_{rc}	0.208	m
Width of half track	l_{ht}	0.808	m
Installation ratio	R_{SD}	0.56	-
Rim radius of road wheel	r_w	0.341	m
Unloaded spring-damper length	l_{SD0}	0.389	m
Equilibruim wheel camber angle	θ_{IHy}	-0.023	rad

TABLE III
PARAMETERS OF SINGLE-LINK ACTUATOR [31] AND SERVO DRIVE CONTROL

Parameters	*Value*	*Unit*
PMSM rated power (Kollmorgen AKM33H)	1300	W
PMSM rated torque (Kollmorgen AKM33H)	2.88	N·m
Experimental power limit	500	W
Velocity lower/upper limit (velocity loop)	-3000/+3000	rpm
Velocity proportional gain (velocity loop)	0.083	A/(rad/s)
Velocity integral time (velocity loop)	6	ms
Current lower/upper limit (current loop)	0/+7.5	A
Current proportional gain (current loop)	12.3	V/A
Current integral time (current loop)	0.725	ms
DC bus voltage	320	V
Gearbox ratio	40:1	-
Gearbox effiency	90	%

APPENDIX

See Tables I–III.

REFERENCES

[1] R. N. Jazar, *Vehicle Dynamics: Theory and Application*. New York, NY, USA: Springer, 2013.

[2] R. S. Sharp and D. A. Crolla, "Road vehicle suspension system design—A review," *Vehicle Syst. Dyn.*, vol. 16, no. 3, pp. 167–192, 1987.

[3] E. M. Elbeheiry, D. Karnopp, M. Elaraby, and A. M. Abdelraaouf, "Advanced ground vehicle suspension systems—A classified bibliography," *Vehicle Syst. Dyn.*, vol. 24, no. 3, pp. 231–258, 1995.

[4] C. Gohrle, A. Schindler, A. Wagner, and O. Sawodny, "Design and vehicle implementation of preview active suspension controllers," *IEEE Trans. Control Syst. Technol.*, vol. 22, no. 3, pp. 1135–1142, May 2014.

[5] S. Evangelou, C. Kneip, D. Dini, O. De Meerschman, C. Palas, and A. Tocatlian, "Variable-geometry suspension apparatus and vehicle comprising such apparatus," U.S. Patent 9 026 309, May 5, 2015.

[6] C. Arana, S. A. Evangelou, and D. Dini, "Series active variable geometry suspension for road vehicles," *IEEE/ASME Trans. Mechatronics*, vol. 20, no. 1, pp. 361–372, Feb. 2015.

[7] C. Arana, S. A. Evangelou, and D. Dini, "Car attitude control by series mechatronic suspension," *IFAC Proc. Volumes*, vol. 47, no. 3, pp. 10688–10693, 2014.

[8] C. Arana, S. A. Evangelou, and D. Dini, "Series active variable geometry suspension application to chassis attitude control," *IEEE/ASME Trans. Mechatronics*, vol. 21, no. 1, pp. 518–530, Feb. 2016.

[9] C. Arana, S. A. Evangelou, and D. Dini, "Pitch angle reduction for cars under acceleration and braking by active variable geometry suspension," in *Proc. IEEE 51st IEEE Conf. Decision Control (CDC)*, Dec. 2012, pp. 4390–4395.

[10] C. Arana, S. A. Evangelou, and D. Dini, "Series active variable geometry suspension application to comfort enhancement," *Control Eng. Pract.*, vol. 59, pp. 111–126, Feb. 2017.

[11] C. R. Arana, "Active variable geometry suspension for cars," Ph.D. dissertation, Dept. Elect. Electron. Eng., Mech. Eng., Imperial College London, London, U.K., 2015.

[12] C. Cheng, S. A. Evangelou, C. Arana, and D. Dini, "Active variable geometry suspension robust control for improved vehicle ride comfort and road holding," in *Proc. Amer. Control Conf. (ACC)*, Jul. 2015, pp. 3440–3446.

[13] S.-J. Huang and W.-C. Lin, "Adaptive fuzzy controller with sliding surface for vehicle suspension control," *IEEE Trans. Fuzzy Syst.*, vol. 11, no. 4, pp. 550–559, Aug. 2003.

[14] D. Fischer and R. Isermann, "Mechatronic semi-active and active vehicle suspensions," *Control Eng. Pract.*, vol. 12, no. 11, pp. 1353–1367, 2004.

[15] C. Lauwerys, J. Swevers, and P. Sas, "Robust linear control of an active suspension on a quarter car test-rig," *Control Eng. Pract.*, vol. 13, no. 5, pp. 577–586, 2005.

[16] Y. Zhang and A. Alleyne, "A practical and effective approach to active suspension control," *Vehicle Syst. Dyn.*, vol. 43, no. 5, pp. 305–330, 2005.

[17] F. Kou and Z. Fang, "An experimental investigation into the design of vehicle fuzzy active suspension," in *Proc. IEEE Int. Conf. Autom. Logistics*, Aug. 2007, pp. 959–963.

[18] A. Kruczek, A. Stribrsky, J. Honc, and M. Hlinovsky, "Controller choice for car active suspension," *Int. J. Mech.*, vol. 3, no. 4, pp. 61–68, 2010.

[19] G. Priyandoko, M. Mailah, and H. Jamaluddin, "Vehicle active suspension system using skyhook adaptive neuro active force control," *Mech. Syst. Signal Process.*, vol. 23, no. 3, pp. 855–868, 2009.

[20] S. Lee and W.-J. Kim, "Active suspension control with direct-drive tubular linear brushless permanent-magnet motor," *IEEE Trans. Control Syst. Technol.*, vol. 18, no. 4, pp. 859–870, Jul. 2010.

[21] D. Maher and P. Young, "An insight into linear quarter car model accuracy," *Vehicle Syst. Dyn.*, vol. 49, no. 3, pp. 463–480, 2011.

[22] B. L. J. Gysen, J. J. H. Paulides, J. L. G. Janssen, and E. A. Lomonova, "Active electromagnetic suspension system for improved vehicle dynamics," *IEEE Trans. Veh. Technol.*, vol. 59, no. 3, pp. 1156–1163, Mar. 2010.

[23] J. C. Dixon, *Suspension Geometry and Computation*. Hoboken, NJ, USA: Wiley, 2009.

[24] M. Yu, S. A. Evangelou, and D. Dini, "Model identification and control for a quarter car test rig of series active variable geometry suspension," *IFAC-PapersOnLine*, vol. 50, no. 1, pp. 3376–3381, 2017.

[25] D. Crolla, "Vehicle dynamics-theory into practice," *Proc. Inst. Mech. Eng. D, J. Automobile Eng.*, vol. 210, pp. 83–94, Apr. 1996.

[26] R. Rajamani, *Vehicle Dynamics and Control*. New York, NY, USA: Springer, 2011.

[27] K. Zhou and J. C. Doyle, *Essentials of Robust Control*. Upper Saddle River, NJ, USA: Prentice-Hall, 1998.

[28] A. Hughes, *Electric Motors and Drives*. Amsterdam, The Netherlands: Elsevier, 2006.

[29] S. Morimoto, Y. Tong, Y. Takeda, and T. Hirasa, "Loss minimization control of permanent magnet synchronous motor drives," *IEEE Trans. Ind. Electron.*, vol. 41, no. 5, pp. 511–517, Oct. 1994.

[30] P. Pillay and R. Krishnan, "Modeling, simulation, and analysis of permanent-magnet motor drives. I. The permanent-magnet synchronous motor drive," *IEEE Trans. Ind. Appl.*, vol. 25, no. 2, pp. 265–273, Mar. 1989.
[31] (2014). *Kollmorgen AKM Servomotor Selection Guide*, Kollmorgen Corp., Radford, VA, USA. [Online]. Available: http://www.kollmorgen.com
[32] *AKD User Guide—Kollmorgen*, Kollmorgen Corp., Radford VA, USA, 2014. [Online]. Available: http://www.kollmorgen.com
[33] (2010). *NI cRIO-9022 User Manual and Specifications*, Nat. Instrum., Austin, TX, USA. [Online]. Available: http://www.ni.com
[34] (1997). *Mechanical Vibration and Shock—Evaluation of Human Exposure to Whole-Body Vibration—Part 1: General Requirements*, ISO Standard 2631-1:1997, ISO.
[35] (1995). *Mechanical Vibration—Road Surface Profiles—Reporting of Measured Data*, ISO Standard 8608:1995, ISO.

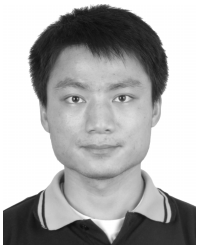

Min Yu (S'16) received the B.Sc. degree in mechanical engineering from Xi'an Jiaotong University, Xi'an, China, in 2011, the M.Sc. degree in mechatronic control engineering from Zhejiang University, Hangzhou, China, in 2014. He is currently pursuing the Ph.D. degree with the Department of electrical and electronic engineering, Imperial College London, London, U.K.

His current research interests include vehicle dynamics and control, mechatronic system modelings, simulation, and experimental validation.

Carlos Arana received the B.A./M.Eng. degree in industrial engineering and the M.Sc. degree in applied and computational mechanical engineering from the Public University of Navarre, Pamplona, Spain, in 2008 and 2009, respectively, and the M.Sc. and Ph.D. degrees from Imperial College London, London, U.K., in 2011 and 2015, respectively.

From 2008 to 2010, he was a Mechanical Engineer with Acciona Windpower, Navarre, Spain. He is currently with das-Nano, Navarra.

Simos A. Evangelou (M'05–SM'17) received the B.A./M.Eng. degree in electrical and information sciences from the University of Cambridge, Cambridge, U.K., in 1999, and the Ph.D. degree in control engineering from Imperial College London, London, U.K., in 2004.

He joined the Departments of mechanical and electrical and electronic engineering, Imperial College London, in 2006, where he is currently a Senior Lecturer with the Department of electrical and electronic engineering.

Dr. Evangelou is a member of the IFAC Technical Committee Automotive Control and on the editorial board of international journals and conferences, including the IEEE Control Systems Society Conference Editorial Board. He is a member of ASME and IET and a fellow of the Higher Education Academy.

Daniele Dini received the M.Eng. degree in mechanical engineering from the Politecnico di Bari, Bari, Italy, in 2000, and the D.Phil. degree in engineering science from the University of Oxford, Oxford, U.K., in 2004.

He joined the Department of Mechanical Engineering, Imperial College London, London, U.K., in 2006, where he is currently the Head of the Tribology Group.

Prof. Dini is a Chartered Engineer, a fellow of IMechE and the Higher Education Academy, a member of the ASME, STLE, and a number of editorial boards of international journals, and the Chairman of the IMechE Tribology Group.